Rheo-Dielectric Responses of Entangled cis-Polyisoprene under Uniform Steady Shear and LAOS

ARTICLE *in* MACROMOLECULES · DECEMBER 2013

Impact Factor: 5.8 · DOI: 10.1021/ma402100t

5 AUTHORS, INCLUDING:

Yuichi Masubuchi
Nagoya University
139 PUBLICATIONS **1,420** CITATIONS

Macromolecules

Article

pubs.acs.org/Macromolecules

Rheo-Dielectric Responses of Entangled *cis*-Polyisoprene under Uniform Steady Shear and LAOS

Kazushi Horio,[†] Takashi Uneyama,[‡] Yumi Matsumiya,[†] Yuichi Masubuchi,[†] and Hiroshi Watanabe[†,*]

[†]Institute for Chemical Research, Kyoto University, Uji, Kyoto 611-0011, Japan

[‡]School of Natural System, College of Science and Engineering, Kanazawa University, Kanazawa, Ishikawa 920-1192, Japan

Supporting Information

ABSTRACT: *cis*-Polyisoprene (PI) has type-A dipoles parallel along the chain backbone so that its large-scale (global) motion over the end-to-end distance activates slow dielectric relaxation. This relaxation was examined for entangled solutions of linear and star-branched PI under steady shear and large-amplitude oscillatory strain. For linear PI, the dielectric relaxation (detecting the end-to-end fluctuation in the shear gradient direction) was hardly affected by the steady shear in a range of Weissenberg number examined, $Wi = \dot{\gamma}\tau_G <$ 7 with $\dot{\gamma}$ and τ_G being the shear rate and the terminal relaxation time in the linear regime, whereas the viscosity η exhibited considerable thinning at those $\dot{\gamma}$. In contrast, for star PI, the dielectric relaxation was moderately accelerated by the steady shear in a similar range of *Wi* but this acceleration was considerably less significant compared to the thinning of η. These rheo-dielectric features, noted also in a previous study, emerged under uniform shear without shear-banding and/or secondary flow, as confirmed in this study from particle tracking velocimetry. Thus, the rheo-dielectric difference between the linear and star PI suggests an essential difference of the entanglement dynamics of linear and star chains (without disturbance from the flow instability), which possibly reflects, at least partly, the constraint release effect at equilibrium being saturated for linear chains but not for star chains. The rheo-dielectric behavior of the linear and star PI chains was also examined under uniform, large amplitude oscillatory strain (LAOS). The relaxational current I_{relax} under rectangular electric field exhibited oscillatory decay with the main oscillation period being close to π/Ω (Ω = LAOS angular frequency). This behavior lent support to the previous analysis based on the Green−Kubo theorem (Uneyama et al. *J. Polym. Sci. Part B: Polym. Phys.* **2009**, *47*, 1039). The decay of the nonoscillating part of I_{relax} appeared to be rather insensitive to LAOS, which was in harmony with the behavior observed under steady shear.

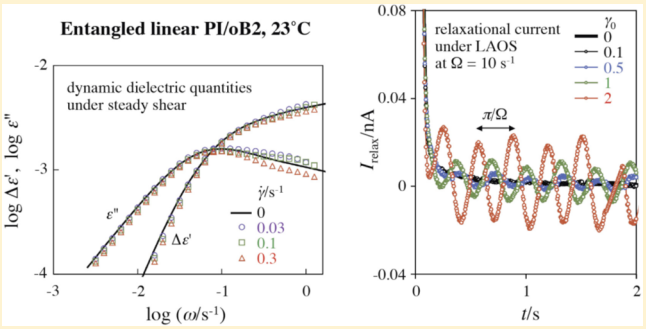

1. INTRODUCTION

Entanglement dynamics under fast flow/large strain is one of the most challenging research subjects in polymer physics. Nonlinear viscoelastic features of entangled polymers, for example, shear-thinning of viscosity under fast steady shear and nonlinear damping of relaxation modulus under large step strain, reflect nonequilibrium chain conformation/dynamics under respective conditions, and the molecular origin(s) of these features has been extensively investigated.[1−11] Large orientation/stretch of the chain due to the flow/strain and successive chain contraction (when allowed) have been considered to be the origin of the nonlinear features. Specifically, the chain contraction after the (transient) stretch releases entanglements to activate nonlinear relaxation. In the context of the widely utilized tube model, this mechanism of relaxation is modeled as "convective constraint release (CCR)".[6−8] The nonlinear viscoelastic behavior, including the shear thinning of viscosity, is considerably well described by the refined tube model(s) incorporating the CCR mechanism.[7−9]

However, a problem(s) still remains for this description. The CCR mechanism itself reduces the average number of entanglements *per* chain thereby accelerating the large-scale (global) motion/relaxation of the chain and decreasing the viscosity. For *cis*-polyisoprene (PI) having type-A dipoles parallel along the chain backbone, this motion has been directly examined through dielectric experiments under steady shear utilizing cone and plate electrodes:[12] The rheo-dielectric data thus obtained for entangled linear PI solutions were hardly affected by the shear at rates $\dot{\gamma}$ higher than the equilibrium terminal relaxation frequency ω_G but lower than the Rouse frequency ω_R. In contrast, the viscosity η exhibited significant thinning in the same range of $\dot{\gamma}$. These results suggest that the nonlinear thinning of viscosity (and the other nonlinear features explained above) is not so straightforwardly related to the CCR mechanism that should unavoidably accelerate the rheo-dielectric relaxation of PI.[6,7,9,13]

In fact, the problem becomes more complicated *if* the steady shear is not uniform due to shear-banding and/or secondary

Received: October 11, 2013
Revised: December 7, 2013
Published: December 16, 2013

flow. Such nonuniformity of flow has been reported for highly entangled melts/solutions at $\dot{\gamma} > \omega_G$,[14−16] but the flow profile was not examined in the previous rheo-dielectric study[12] (reported earlier than refs 14−16.). *If* the shear-banding occurs in the shear gradient direction, the rheo-dielectric data detect the harmonic average of the responses from PI in the fast and slow bands weighed by the volume fraction of respective bands. Then, the observed lack of the shear-induced acceleration of the data did not necessarily mean the lack of acceleration of the global motion *if* the fast band had just a small volume fraction and the chain dynamics in the slow band was close to the equilibrium dynamics. The same problem arises if the wall slippage occurs and/or a slipping place is formed in the material.

Thus, we revisited this problem. Specifically, we examined rheo-dielectric behavior of an entangled solution of linear PI and also its flow velocity profile. For comparison, the rheo-dielectric behavior and flow profile were examined also for an entangled solution of star-branched PI. It turned out that the flow remained homogeneous (no shear-banding) in the shear-thinning regime examined ($\dot{\gamma} < 8.5\omega_G$), but the shear effect on the rheo-dielectric behavior was less significant (negligible and just moderate acceleration for linear and star PI, respectively, as observed previously[12]) compared to the effect on the viscosity. This paper presents details of these results and discusses the difference between the linear and star PI.

In addition, we also examined the rheo-dielectric behavior and flow profile of the linear and star PI solutions under large amplitude oscillatory strain (LAOS). The data for both linear and star PI suggested that the conformational distribution of the chains is coupled with LAOS and thus the rheo-dielectric response against a constant electric field is composed of a monotonically decaying part and an oscillating part. This result lends support to a previous theoretical analysis[13] based on the Green−Kubo theorem. The monotonic part of the rheo-dielectric response was rather insensitive to LAOS, which was consistent with the results obtained under steady shear. Details of these results are also presented in this paper.

II. EXPERIMENTAL SECTION

II.1. Materials. Linear and 6-arm star-branched PI samples having high molecular weights (M) were utilized. The star PI sample was synthesized/fractionated/characterized in a previous study.[12] This sample, containing a small amount (~0.1% to PI) of antioxidant, butylhydroxytoluene (BHT), has been sealed in Ar and kept in a deep freezer until use.

The linear PI sample was living-anionically polymerized in this study. Benzene and *s*-butyllithium were utilized as the polymerization solvent and initiator. The polymerized sample was fractionated twice from benzene/methanol mixtures, and a final benzene solution was dried in high vacuum at 50 °C for 2 days to recover the purified sample. A small amount of BHT (~0.02 wt % to the PI sample) was added to the final benzene solution.

The linear PI sample thus obtained was characterized with GPC (CO-8020 and DP-8020; Tosoh) equipped with a refractive index (RI) monitor (RI-8020, Tosoh) and a low-angle laser light scattering (LALLS) detector (Viscotek 270, Malvern) connected in series: Its weight-average molecular weight M_w and polydispersity index M_w/M_n were evaluated from the LALLS/RI signal ratio measured at respective sections of elution volume. The elution solvent was tetrahydrofuran (THF), and monodisperse linear PI samples synthesized/characterized in the previous studies[17,18] were utilized as the RI/LALLS standards. The GPC trace was also examined for the previously synthesized star PI sample[12] to confirm lack of degradation during the storage.

Table 1 summarizes the molecular characteristics of the linear and star PI samples thus determined. The materials subjected to rheo-

Table 1. Molecular Characteristics of PI Samples

	$10^{-4}M_w$	M_w/M_n
linear PI	144	1.12
star PI[a]	17.9 (for arm)	1.03

[a]Synthesized/characterized in ref 12.

dielectric measurements under steady shear and large amplitude oscillatory strain (LAOS) were solutions of linear and star PI samples in an oligomeric butadiene (oB2; Nisseki PB2000 obtained from Nisseki Co; 1,2-*vinyl*:1,4-*cis*/*trans* =83:17, $M_w = 2 \times 10^3$, $M_w/M_n \cong 2$).[12,19] The PI concentration was 5 and 20 wt % for the linear and star PI solutions, respectively. These solutions were prepared by first dissolving prescribed masses of PI and oB2 samples in benzene (at a concentration ~5 wt %) and then allowing benzene to thoroughly evaporate, first in ambient condition for 1 day and then in high vacuum at 50 °C for 2 days. In addition to the neat PI/oB2 solutions, solutions containing a small amount (600 ppm wt/wt in the solution) of hollow silica particles with the diameter of ≅ 10 μm (HGS-10, Deantec Dynamic) were also prepared with the same method. These particles served as the tracer for detecting the shear velocity profile in the samples, as in the experiment by Wang et al.[15]

II.2. Measurements. *Dielectric Measurements.* For the linear and star PI solutions in oB2 containing *no* tracer particles, dielectric measurements were conducted with an impedance analyzer/dielectric interface system (1260 and 1296; Solartron) and a homemade circuit, the latter being comprising of a function generator (1941, Wave Factory), an electrometer (6485 Picoammeter, Keithley), and a digital recorder (DL708E, Yokogawa). (No dielectric measurement was made for the solution containing the particles because the particles introduced ionic impurities to disturb the measurements.) The former system was utilized for measurements under a sinusoidal electric field (at angular frequencies $\omega = 2\pi f = 0.1-10^5$ s^{-1}, with f being the frequency in Hz unit), and the latter, for measurements under rectangular electric field on the basis of the adsorption current (AdC) method described previously.[12,20]

The measurements utilized cone and plate electrodes mounted on a laboratory rheometer (ARES, TA Instruments). The electrodes, designed/machined in the previous study,[12] had a diameter of 5.0 cm and the gap angle of 2.0°, and the cone had a truncated head to avoid contact with the plate electrode (counter electrode). The cone and plate electrodes, respectively, were attached to the driving shaft and the torque detector of the rheometer, and thus the cone electrode rotated during the rheo-dielectric measurements under steady shear, whereas the plate electrode was fixed. The inner part and outer edge of the cone, mutually insulated by a Teflon block, served as the main and guard electrodes, and the inner (main) electrode was connected to a metallic contact ring immersed in a mercury reservoir so that the rotation of this electrode did not disturb the measurement. (The impedance analyzer/dielectric interface system and the homemade circuit explained above were connected to the mercury reservoir, and the rotation of the contact ring in this reservoir gave negligibly small electrical noise for the signal from the sheared samples.) Further details of the electrodes were described in ref 12.

The rheo-dielectric measurements under steady shear flow and large amplitude oscillatory shear strain (LAOS) were conducted with the AdC method for the linear and star PI solutions at reference temperatures T_r = 23 and 18 °C (room temperature), respectively.

The measurements at equilibrium (no flow/LAOS) were made with the AdC method at these T_r and also with the standard method (utilizing the sinusoidal electric field) at several temperatures including those T_r. Time−temperature superposition was valid, and the data obtained with the standard method were reduced at T_r.

Particle Tracking Velocimetry.[15] The PI/oB2 solutions containing the tracer particles were subjected to the steady shear/LAOS in the above cone-and-plate geometry (electrodes). The local velocity profile

dx.doi.org/10.1021/ma402100t | Macromolecules 2014, 47, 246−255

therein was determined by tracing the particles with a high-speed video camera (VW-6000, Keyence Corporation). The camera was set just beside the cone-and-plate geometry, and its focus was placed on the geometry edge to record the trajectories of the particles nearby the edge. The video images of those particles were digitized to determine the particle position h (height in the cone-and-plate gap measured from the plate surface) and the velocity v in the shear direction. The viscoelastic data explained below were indistinguishable for the solutions with and without particles because the particles were dilute. Thus, we utilized the velocity profile of the particles as the flow profile in the particle-free solutions.

Rheological Measurements. For the linear and star PI/oB2 solutions at respective reference temperatures, T_r = 23 and 18 °C, steady shear and LAOS measurements were conducted with the cone-and-plate geometry (electrodes) mounted on the rheometer. These rheological measurements were made for the solutions with and without the tracer particles, and the rheo-dielectric measurement was simultaneously conducted for the particle-free solutions. The rheological data agreed for the solutions with and without the particles. Thus, the dilute tracer particles had no detectable effect on the rheological behavior of the solutions, and quite possibly no effect on the flow profile as well. For this reason, we utilized the velocity profile of the particles as the flow profile in the particle-free solutions for which the rheo-dielectric behavior was examined.

For comparison, the above rheological measurements were made also with a smaller cone−plate geometry (standard accessory of ARES) having the diameter of 2.5 cm and the gap angle of 5.73° (0.1 rad). The rheological data obtained with this geometry agreed with those from the large geometry utilized for the rheo-dielectric measurements, confirming accuracy of the data obtained with the latter geometry. In addition, dynamic viscoelastic measurements at a small strain amplitude (γ_0 = 0.1 in the linear response regime) were made for the particle-free solutions at several temperatures including the reference temperature T_r explained above. The time−temperature superposition was valid for the storage and loss moduli G' and G'' thus measured, and the shift factor a_T was identical to that obtained for the dielectric data. These moduli data were reduced/compared at T_r.

3. RESULTS AND DISCUSSION

3.1. Overview of Linear Behavior. In the PI/oB2 solutions examined, the number of entanglements *per* linear PI chain and/or span (two arms) of the star PI are evaluated as

$$N = M/(M_e^\circ/\phi^{1.3}) \cong 5.9 \text{ for linear PI (in 5 wt \% solution)} \quad (1a)$$

$$N_{span} = 2M_{arm}/(M_e^\circ/\phi^{1.3}) \cong 8.8 \text{ for star PI (in 20 wt \% solution)} \quad (1b)$$

where M_e° denotes the entanglement molecular weight of bulk PI (=5 × 10^3)[21] and ϕ is the volume fraction of PI in the solution. Thus, in the solutions the linear and star PI chains were in a moderately entangled state.

For these linear and star PI solutions at T_r = 23 and 18 °C, respectively, Figures 1 and 2 show double logarithmic plots of the linear viscoelastic storage and loss moduli, $G'(\omega)$ and $G''(\omega)$, the decrease of the dynamic dielectric constant from the static permittivity, $\Delta\varepsilon'(\omega) \equiv \varepsilon'(0) - \varepsilon'(\omega)$, and the dielectric loss $\varepsilon''(\omega)$ against the angular frequency ω. The filled and unfilled circles, respectively, indicate the dielectric data obtained with the standard method (utilizing the sinusoidal electric field) and with the adsorption current (AdC) method (utilizing the rectangular electric field) explained in the Experimental Section. With the latter method, the relaxational part of the adsorption current $I_{relax}(t)$, obtained by subtracting a direct current contribution due to ionic impurities, was Fourier-transformed to give $\Delta\varepsilon'(\omega)$ and $\varepsilon''(\omega)$, as fully explained in the

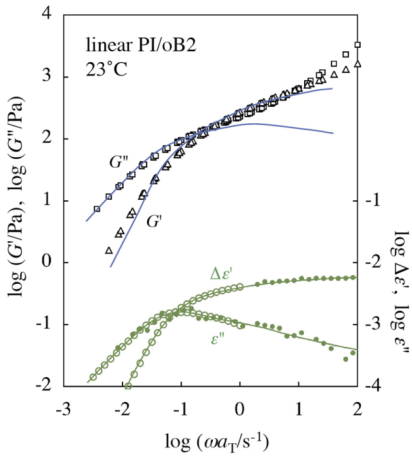

Figure 1. Viscoelastic and dielectric behavior of linear PI/oB2 solution (5 wt %) at 23 °C. Thin blue curves indicate the viscoelastic moduli calculated from the dielectric data on the basis of full-DTD relationship.

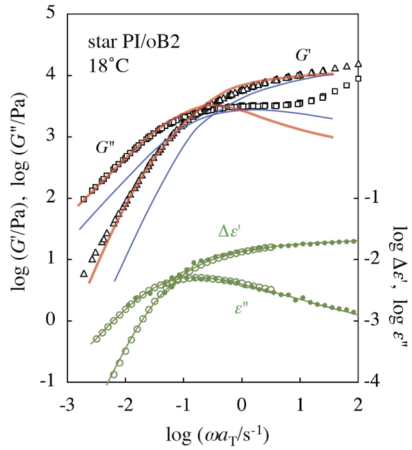

Figure 2. Viscoelastic and dielectric behavior of star PI/oB2 solution (20 wt %) at 18 °C. Thin blue and thick red curves, respectively, indicate the viscoelastic moduli calculated from the dielectric data on the basis of full-DTD and partial-DTD relationships.

previous papers.[12,20] (The $I_{relax}(t)$ data are later shown in Figures 10 and 11.) These $\Delta\varepsilon'(\omega)$ and $\varepsilon''(\omega)$ data agree well with the data obtained with the standard method.

The viscoelastic and dielectric quantities examined in Figures 1 and 2 are defined within the same framework of linear stimulus-response theory and are related to respective relaxation functions as[22,23]

$$G^*(\omega) \equiv G'(\omega) + iG''(\omega) = i\omega G_0 \int_0^\infty \mu(t) e^{-i\omega t}\, dt \quad (i = \sqrt{-1}) \quad (2)$$

$$\Delta\varepsilon^*(\omega) \equiv \Delta\varepsilon'(\omega) + i\varepsilon''(\omega) = i\omega\Delta\varepsilon \int_0^\infty \Phi(t) e^{-i\omega t}\, dt \quad (3)$$

In eq 2, G_0 and $\mu(t)$ are the viscoelastic relaxation intensity (initial modulus) and normalized relaxation modulus ($\mu(0)$ = 1), and $\Delta\varepsilon$ and $\Phi(t)$ in eq 3, the dielectric relaxation intensity and the normalized dielectric relaxation function ($\Phi(0)$ = 1). Thus, $G^*(\omega)$ and $\Delta\varepsilon^*(\omega)$ exhibit the same power-law behavior at sufficiently low ω, $G'(\omega)$, $\Delta\varepsilon'(\omega) \propto \omega^2$ and $G''(\omega)$, $\varepsilon''(\omega) \propto$

dx.doi.org/10.1021/ma402100t | Macromolecules 2014, 47, 246−255

ω, as noted in Figures 1 and 2. In addition, for PI having type-A dipoles parallel along the chain backbone, $\Phi(t)$ in the linear regime is given by the autocorrelation functions:[13,22−24]

$$\Phi(t) = \frac{\langle R_y(t)R_y(0)\rangle_{eq}}{\langle R_y{}^2\rangle_{eq}} \quad \text{(for linear PI)} \tag{4}$$

$$\Phi(t) = \frac{\sum_{\alpha,\alpha'=1}^{q}\langle R_{arm,y}^{[\alpha]}(t)R_{arm,y}^{[\alpha']}(0)\rangle_{eq}}{q\langle R_{arm,y}{}^2\rangle_{eq}} \quad \text{(for } q\text{-arm star PI)} \tag{5}$$

In eq 4, $R_y(t)$ indicates the component of the end-to-end vector of the linear chain in the direction of the electric field (chosen to be y direction), and $\langle\cdots\rangle_{eq}$ specifies the ensemble average at equilibrium. Similarly, $R_{arm,y}^{[\alpha]}(t)$ in eq 5 denotes the y component of the end-to-branching point vector of the αth arm of the star chain (composed of q arms). Thus, the large-scale motion of linear/star PI chains results in the dielectric relaxation in the same range of frequency (or time) as that for the viscoelastic relaxation, as noted in Figures 1 and 2.

Previous studies compared viscoelastic and dielectric data of bulk PI to reveal that the constraint release (CR) mechanism loosens the entanglement constraint in monodisperse systems and this loosening can be cast in the molecular picture of dynamic tube dilation (DTD) within the context of the tube model:[17,20,23,25−29] The CR mechanism allows polymer chain to explore local conformations within a certain length scale $a_{CR}(t)$ (>undilated tube diameter a) according to the focused time scale, and then the tube determining the stress level effectively dilates to a diameter $a_{DTD}(t)$ which does not exceed $a_{CR}(t)$. The CR-equilibration length scale $a_{CR}(t)$ is evaluated from the CR time data, which enabled us to test the DTD picture in a purely empirical way without relying on a specific DTD molecular model.[20,23,26,28,29]

The key quantity in the above test is the survival fraction of the dilated tube, $\varphi'(t)$, that can be evaluated dielectrically for the type-A PI chains ($\varphi'(t)$ essentially coincides with the dielectric relaxation function $\Phi(t)$). In the *full*-DTD picture, the relaxed portion of the chain is regarded as a "solvent", and consequently, $\varphi'(t)$, as the polymer concentration in a solution, so that the tube for bulk PI is considered to *fully* dilate to the diameter in the solution, $a_{full\text{-}DTD}(t) = a\{\varphi'(t)\}^{-d/2}$ with d being the dilation exponent (≅1.3 for PI). This full-DTD picture is valid when $a_{full\text{-}DTD}(t) \le a_{CR}(t)$, and the viscoelastic $\mu(t)$ is related to $\varphi'(t)$ as $\mu(t) = \{\varphi'(t)\}^{1+d}$ for this case.[17,20,23,25−29]

For monodisperse linear PI bulk, experiments revealed that the dielectrically evaluated $\varphi'(t)$ data and the $\mu(t)$ data obeyed this full-DTD relationship, and the validity of the prerequisite for this relationship ($a_{full\text{-}DTD}(t) = a\{\varphi'(t)\}^{-d/2} \le a_{CR}(t)$) was confirmed from the $\varphi'(t)$ data and the CR time data, the latter determining $a_{CR}(t)$.[20,23] This result reflects a rather narrow distribution of the relaxation modes of linear PI chains. The narrowly distributed modes leads to just a moderate decay of $\varphi'(t)$ on an increase of t up to the terminal viscoelastic relaxation time τ_G. Consequently, the fully dilated tube diameter remains rather small[12,20,23] ($a_{full\text{-}DTD}(t) \cong 1.7a$ even at $t = \tau_G$),[27] which allows the linear chain to be CR-equilibrated (to explore all local conformations) within the length scale of $a_{full\text{-}DTD}(t)$ in time.

In contrast, for monodisperse star PI bulk, experiments indicated $a_{full\text{-}DTD}(t) > a_{CR}(t)$ at intermediate to long t and the full-DTD relationship between $\varphi'(t)$ and $\mu(t)$ fails at those t.[20,26,28,29] This failure is related to broadly distributed relaxation modes of star PI. Namely, intensive fast modes significantly decrease $\varphi'(t)$ at short t thereby not allowing $a_{full\text{-}DTD}(t)$ to stay below $a_{CR}(t)$ at intermediate to long t. In addition, Milner−McLeish model combining the star arm retraction with the full-DTD picture excellently describes the viscoelastic data of star PI, but the same model with the same parameter values does not consistently describe the dielectric data; see Figures 9 and 10 of ref 20 and Figure 8 of ref 23. Thus, the failure of the full-DTD picture for star PI has been noted also for the molecular model, and the origin of this failure has been theoretically analyzed by focusing on a high dimensional Kramers process that models the arm retraction in the dilating tube.[2]

The failure of the full-DTD picture for star PI suggests that the star arm explores the local conformations within a length scale $a_{partial\text{-}DTD}(t) = \mathbf{min}\{a_{full\text{-}DTD}(t), a_{CR}(t)\}$. In fact, experiments indicated that the $\mu(t)$ and $\varphi'(t)$ data of star PI obey a relationship deduced from this partial-DTD picture, $\mu(t) = \varphi'(t)/\beta(t)$ with $\beta(t) = \{a_{partial\text{-}DTD}(t)/a\}^{1/2}$,[23,28,29] which lends support to the above argument of CR-equilibration.

The above features, established for bulk PI, are expected to be observed also for the linear and star PI chains in the oB2 solutions examined in this study. Thus, we utilized the previous method[17,28] to analyze the dielectric data of those chains (green plots in Figures 1 and 2) and calculate the viscoelastic moduli for the cases of full- and partial-DTD. Details of this analysis are summarized in the Supporting Information. The moduli thus obtained for the full-DTD case are shown in Figures 1 and 2 with the thin blue curves, and those for the partial-DTD case, with the thick red curves. Clearly, linear PI obeys the full-DTD relationship, whereas this relationship fails and the partial DTD relationship is valid for star PI, both in the dominant part of the terminal relaxation process. (These relationships do not account for the local Rouse relaxation within the entanglement segment, and their validity is limited to middle-to-low ω where the local Rouse relaxation hardly contributed to the moduli data.)

Thus, the validity and invalidity of the full-DTD picture have been confirmed for the linear and star PI in the solutions. This result suggests that an *extra* room for tube dilation remains for the star PI but not for linear PI in the linear viscoelastic regime (at equilibrium). This difference between the linear and star PI at equilibrium could be a key for understanding a difference in their rheo-dielectric behavior under nonequilibrium shear flow,[12] as discussed in the following sections.

3.2. Rheo-Dielectric Behavior under Steady Shear Flow. *3.2.1. Experimental Observation.* Figures 3 and 4, respectively, show the $\Delta\varepsilon'(\omega)$ and $\varepsilon''(\omega)$ data of the linear and star PI solutions under steady shear flow at the rates $\dot\gamma$ as indicated. (The data were obtained with the AdC method and the relaxational part of the adsorption current was Fourier transformed to obtain $\Delta\varepsilon'(\omega)$ and $\varepsilon''(\omega)$, as explained for Figures 1 and 2.) The Weissenberg number $\dot\gamma\tau_G(0)$ defined with respect to the terminal viscoelastic relaxation time in the linear regime, $\tau_G(0) = [G'/\omega G'']_{\omega\to 0}$ (=22 and 34 s for linear and star PI), ranges from 0.7 to 6.7 for linear PI and from 1.0 to 8.5 for star PI. (Note that $G'(\omega) \propto \omega^2$ and $G''(\omega) \propto \omega$ at ω sufficiently lower than $\tau_G(0)$, as explained earlier for eq 2.) For comparison, the data at equilibrium ($\dot\gamma = 0$; already shown in Figures 1 and 2) are reproduced with the black solid curves.

The Green−Kubo (GK) theorem ensures that the dielectric signal of PI *at equilibrium* detects the end-to-end (or end-to-

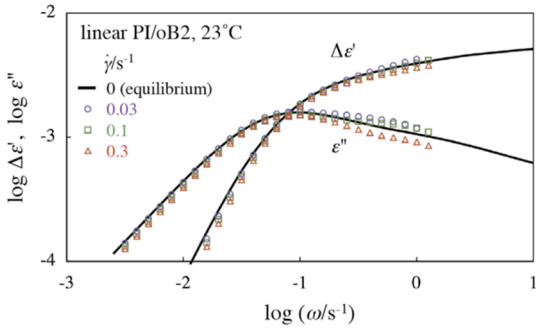

Figure 3. Rheo-dielectric behavior of linear PI/oB2 solution (5 wt %) at 23 °C.

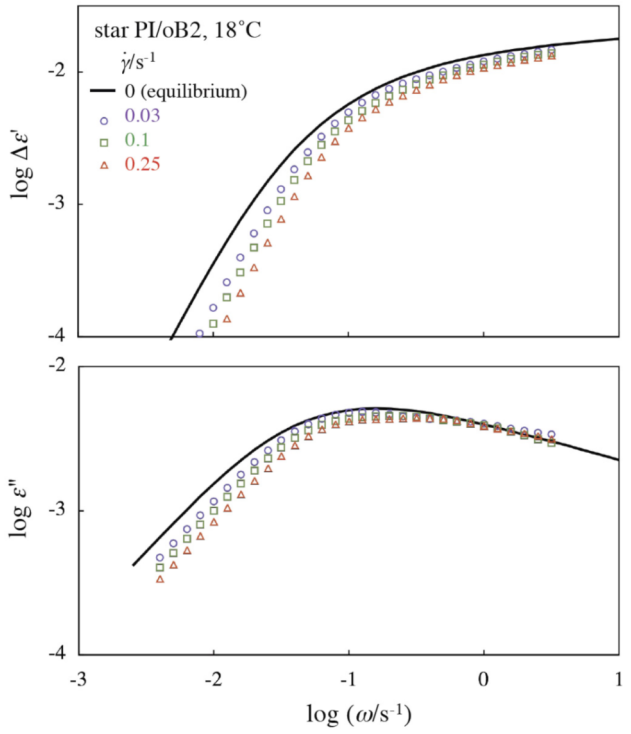

Figure 4. Rheo-dielectric behavior of star PI/oB2 solution (20 wt %) at 18 °C.

branching point) fluctuation and is described by eqs 4 and 5.[13,22−24] This theorem does not necessarily hold rigorously in the nonequilibrium state. However, a previous analysis based on the Langevin equation suggests that the theorem is satisfactorily valid under steady shear and the dielectric relaxation function $\Phi_{ss}(t)$ is described by eqs 4 and 5 with the average $\langle\cdots\rangle$ being taken under the steady shear.[13] Thus, the data presented in Figures 3 and 4 serve as a rigid basis for discussing the fluctuation in the shear-gradient direction (the direction of the electric field).

This fluctuation is rather insensitive to the steady shear for linear PI but moderately accelerated for star PI, as noted in Figures 3 and 4. This behavior can be quantitatively examined in Figure 5 where the terminal dielectric relaxation time (second moment average relaxation time),[3,22,23] $\tau_\varepsilon = [\Delta\varepsilon'/\omega\varepsilon'']_{\omega\to 0}$, under steady shear is normalized by its equilibrium value $\tau_\varepsilon(0)$ and plotted against the Weissenberg number defined with respect to the terminal relaxation time, $\dot\gamma\tau_G(0)$. For comparison, the viscosity η measured simultaneously with the $\Delta\varepsilon'$ and ε'' data are also shown in a normalized form ($\eta(\dot\gamma)$ data

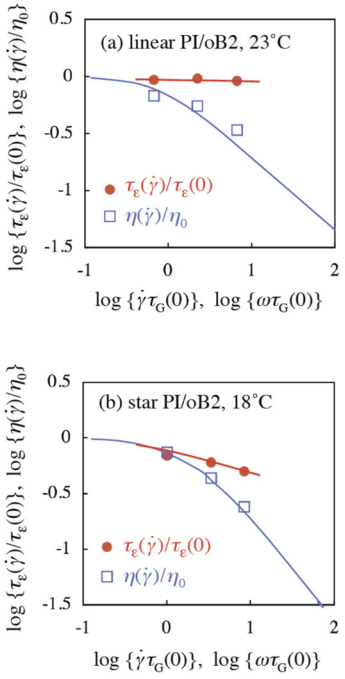

Figure 5. Shear rate dependence of the rheo-dielectric relaxation time (filled red circles) of the linear and star PI solutions. For comparison, plots are shown also for the non-Newtonian viscosity (η; blue squares) and the dynamic viscosity in the linear regime (η'; blue curves).

reduced by the zero-shear viscosity η_0). The thin blue curves indicate the normalized dynamic viscosity $\eta'(\omega)/\eta_0$ ($=G''(\omega)/\omega\eta_0$) plotted against the normalized frequency, $\omega\tau_G(0)$. The viscosity $\eta(\dot\gamma)$ exhibits considerable thinning, and its $\dot\gamma$ dependence is close to the ω dependence of the linear viscoelastic $\eta'(\omega)$ (i.e., the empirical Cox−Merz rule[2,3] is valid). Despite this nonlinear feature of $\eta(\dot\gamma)$, the rheo-dielectric τ_ε of linear PI hardly decreases (by ∼10% at the maximum) in the range of $\dot\gamma$ examined. For star PI, τ_ε exhibits a detectable decrease (by ∼50%), but this decrease is considerably less significant compared to the thinning of $\eta(\dot\gamma)$. All these features are similar to those observed in a previous study.[12]

The flow velocity profile determined by tracing the dilute particles dispersed in the PI solutions is shown in Figure 6, where the particle velocity v is plotted against the particle height h from the fixed part of the rheometer (plate) normalized by the gap H between the cone and plate. Those profiles were obtained in a range of strain $\dot\gamma t$ between 20 and 30 where the stable steady flow (after the stress overshoot) was well achieved. The particles did not affect the viscoelastic data, as explained earlier. For the shear rates examined in Figure 6, the measured profiles (plots) agree, within experimental resolution, with the solid lines that represent the profile for uniform flow associated with no shear banding/no secondary flow. Flow instability due to the edge fracture (partly similar to the shear banding reported in literature[14−16]) was observed for the linear PI solution at $\dot\gamma$ = 0.6 s^{-1}, and a fraction of the solution escaped the cone−plate gap at this $\dot\gamma$.[30] The mild deviation of the plot from the line seen in Figure 6a for $\dot\gamma$ = 0.3 s^{-1} might be attributed to a weak heterogeneity in the flow profile (a pre-effect of such flow instability). However, the lowest local rate evaluated from the least steep part of the plot for $\dot\gamma$ = 0.3 s^{-1}, $\dot\gamma_{local} \cong$ 0.22 s^{-1}, is well above $1/\tau_G(0)$ (= 0.045 s^{-1}) so that the weak heterogeneity, if any, hardly affects the

dx.doi.org/10.1021/ma402100t | Macromolecules 2014, 47, 246−255

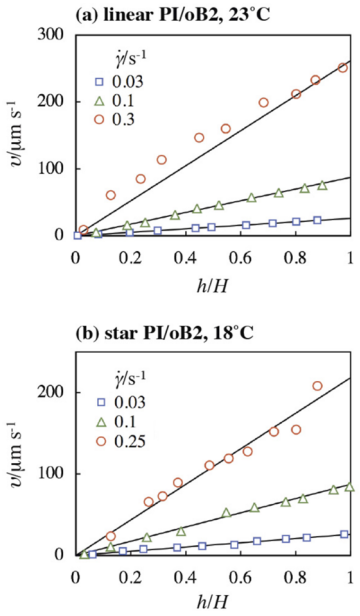

Figure 6. Flow velocity profile in the PI solutions determined with particle tracking velocimetry. The particle velocity in the shear direction, v, is plotted against the particle height h from the fixed plate normalized by the gap H. Solid lines show the profile for uniform flow (no shear banding/no secondary flow).

plot of τ_ε in Figure 5a. Thus, the weak $\dot{\gamma}$ dependence of τ_ε (in particular for linear PI) associated with strong thinning of η reflects a real feature of the chain dynamics under *uniform* flow.

3.2.2. Discussion of Behavior under Steady Shear. Having confirmed that the weak $\dot{\gamma}$ dependence of τ_ε is the real feature under *uniform* flow, we here consider a possible molecular origin(s) of this weak dependence. We can first focus on the convective constraint release (CCR) mechanism[6−9] that is incorporated in the current tube model as the key mechanism to suppress unphysical decrease of the stress on an increase of $\dot{\gamma}$ ($>1/\tau_G(0)$). This mechanism, activating the relaxation on the chain contraction, unavoidably results in a decrease of τ_ε that is similar, in magnitude, to the decrease of η. This strong $\dot{\gamma}$ dependence of τ_ε is directly found in the expression of the relaxation time in the CCR model first proposed by Ianniruberto and Marrucci,[6] $1/\tau_G(\dot{\gamma}) = 1/\tau_G(0) + K\dot{\gamma}$ with the factor K being determined by the chain orientation, and also from detailed calculation based on the current model(s), for example, the Graham−Likhtman−McLeish−Milner (GLaMM) model:[9b] An example of the calculation of this model for the rheo-dielectric response is shown in the Supporting Information. Similarly, a multiple-chain simulation based on a primitive chain network model (NAPLES), that automatically exhibits the CCR behavior, describes the η data but overestimates the $\dot{\gamma}$ dependence of τ_ε.[10,13] Thus, the weak $\dot{\gamma}$ dependence of τ_ε associated with the strong $\dot{\gamma}$ dependence of η cannot be explained just by the CCR mechanism, which suggests necessity of further refinement of the current model/simulation.

In the previous study,[10,13] we proposed a hypothesis that the CCR-induced removal of entanglements of a given chain (probe) is compensated by rapid, *isotropic* reformation of entanglements with the surrounding chains, following the molecular concept of hidden entanglement appearance considered by Ianniruberto and Marrucci.[31] This isotropic reformation leads to, in principle, no change in the orientational anisotropy/stress of the entanglement segments of the probe and thus retains the strong thinning of η, but increases the path length for reptation/arm retraction (toward the length at equilibrium) to reduce the shear effect on τ_ε.

This isotropic entanglement reformation under flow would occur for both linear and star chains. However, at equilibrium, the full-DTD relationship is valid for the linear chain but not for the star chain (cf. Figures 1 and 2). This result suggests that the star chain at equilibrium has an *extra* room for tube dilation compared to the linear chain. Then, under the steady shear, the CCR effect competing with the isotropic entanglement reformation could be stronger for the star chain than for the linear chain to give the moderate $\dot{\gamma}$ dependence of τ_ε for the star chain (that is still weaker than the dependence of η), as discussed previously.[12]

The above hypotheses sound reasonable but do not complete the whole molecular story. First of all, a recent experiment[27] for binary PI/PI blends composed of dilute short probe chains in a matrix of much longer chains suggested that monodisperse linear PI chains at equilibrium exhibit reptation along a partially dilated tube that wriggles in the fully dilated tube. In other words, the full-DTD picture valid for those chains at equilibrium just specifies the relation between the tube survival fraction and the modulus, i.e., the stress level, but does not predict the relaxation time (that is determined by the reptation path length). No corresponding data are available for star PI blends containing dilute short probes, and it remains unknown if the retraction path length of the star arm at equilibrium is shortened by the CR/DTD mechanism more significantly compared to the reptation path length of the linear chain. Thus, the above argument for the difference of τ_ε of the linear and star chains under flow, being based on the validity/invalidity of the full-DTD picture at equilibrium, may need to be refined according to those awaited data for the star chain.

In addition, the segmental friction of those chains may become anisotropic, *if* the chains are *highly oriented* under flow:[32,33] The friction in the shear (x) direction may become smaller than that in the shear gradient (y) direction. If this is the case, the chain motion in the x direction could be accelerated to reduce the orientational anisotropy/stress thereby providing the viscosity with strong $\dot{\gamma}$ dependence, whereas the motion in the y direction could be less accelerated to give $\dot{\gamma}$-insensitive τ_ε. Nevertheless, the difference in the $\dot{\gamma}$ dependence of τ_ε was noted for the linear and star PI in essentially the same range of the Weissenberg number $\dot{\gamma}\tau_G(0)$ where η decreases similarly for linear and star PI (Figure 5). This fact suggests that the frictional anisotropy is not the only factor weakening the $\dot{\gamma}$ dependence of τ_ε.

Thus, the full molecular picture for the rheo-dielectric behavior has not been established. A further study is desired for this problem.

3.3. Rheo-Dielectric Behavior under LAOS. *3.3.1. Behavior Detected with Constant Electric Field.* For the linear and star PI solutions, respectively, parts a and b of Figure 7 show the stationary Lissajou's patterns (stress−strain patterns) obtained under LAOS at the angular frequencies Ω = 1 and 0.1 s^{-1}, respectively. These Ω values were chosen to be well above the terminal viscoelastic relaxation frequency of the solutions determined from the G' and G'' data (cf. Figures 1 and 2), $\omega_G(0) = [\omega G''/G']_{\omega\to 0}$ = 0.045 and 0.029 s^{-1} for linear and star PI, respectively. The LAOS amplitude γ_0 was varied from 0.1 (in the linear regime) to 2 or 4, and the stress $\sigma(t)$ and strain $\gamma(t)$ (= $\gamma_0 \sin \Omega t$) shown in the Lissajou's patterns are

dx.doi.org/10.1021/ma402100t | *Macromolecules* 2014, 47, 246−255

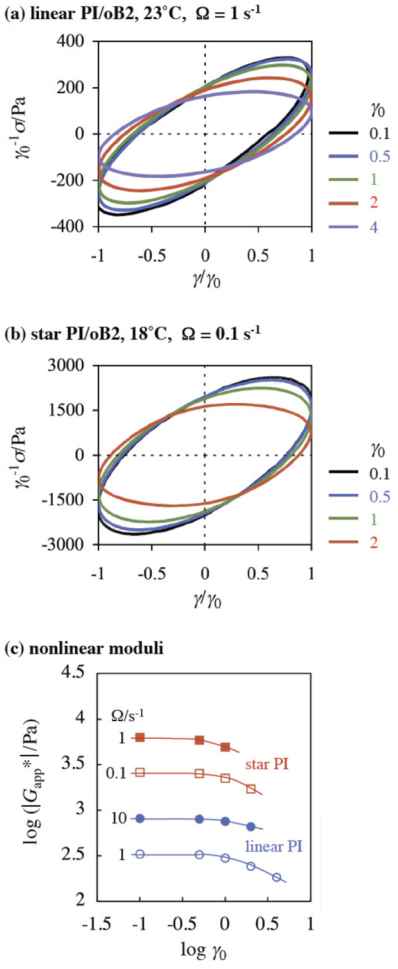

Figure 7. Lisssajou's patterns obtained for linear and star PI solutions under LAOS at the frequency Ω and amplitude γ_0 as indicated (panels a and b). In panel c, the magnitude of apparent modulus (that reduces to the linear viscoelastic modulus for small γ_0) is plotted against γ_0.

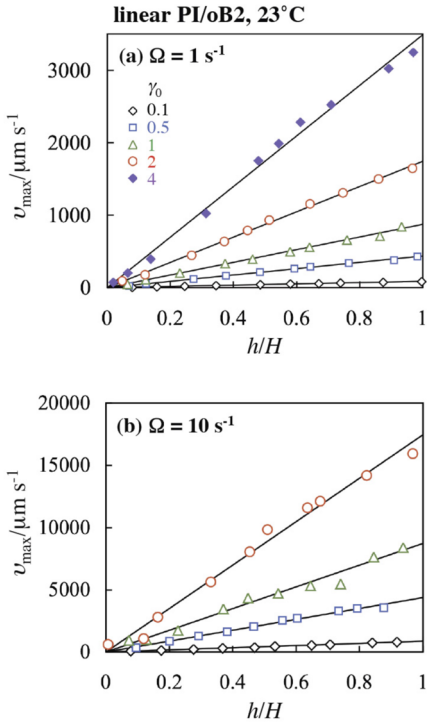

Figure 8. Maximum velocity υ_{max} of particles dispersed in the linear PI solution. υ_{max} is plotted against the particle height h from the fixed plate normalized by the gap H. Solid lines show the maximum velocity realized for uniform oscillatory strain field.

normalized by γ_0. The patterns are distorted from ellipsoid on an increase of $\gamma_0 > 0.5$, and this distortion corresponds to contribution of higher order odd harmonics to $\sigma(t)$ for large γ_0.[34,35]

Nonlinearity under LAOS provides the Lissajou's pattern with not only the distortion but also a decrease of the maximum value of the normalized stress, $\sigma(t)/\gamma_0$, that can be defined as the magnitude of apparent modulus $|G_{app}^*|$. ($|G_{app}^*|$ reduces to the magnitude of the well-defined linear viscoelastic modulus $|G^*|$ under small strains.) In Figure 7c, $|G_{app}^*|$ evaluated from the Lissajou's patterns (a and b) is plotted against the LAOS amplitude γ_0 (unfilled symbols). For comparison, $|G_{app}^*|$ of the linear and star PI solutions obtained at higher Ω are also shown (filled symbols). For both solutions, the decrease of $|G_{app}^*|$ becomes significant for $\gamma_0 > 0.5$. The decrease in this range of γ_0 and at $\Omega > \omega_G$ is well-known for entangled polymers.[34,35]

Uniformity of the strain field under the above LAOS condition was examined by tracing particles in the samples. For the linear PI solution, the particles were clearly observed for all Ω and γ_0 values examined and the particle positions were digitalized/analyzed as explained earlier. This was the case also for the star PI solution (except at $\Omega = 1\ s^{-1}$ and $\gamma_0 = 1$, where the sample surface became wavy and the particles were not clearly observed; no analysis was attempted for this case). It turned out that the oscillation of the particle position was in phase with the macroscopic oscillation of the moving part (cone) of the rheometer, and the maximum velocity υ_{max} of the particles (in the shear direction) was observed when the particles were located at the center of oscillation.

For the linear and star PI solutions, υ_{max} thus determined is shown in Figures 8 and 9, respectively. υ_{max} is plotted against the particle height h from the fixed part of the rheometer (plate) normalized by the gap H between the cone and plate. The solid lines indicate the relationship realized for uniform oscillatory strain field without shear-banding and/or secondary flow,

$$\upsilon_{max} = \frac{h}{H}\gamma_0\theta_{cp}r_p\Omega \tag{6}$$

where r_p and θ_{cp} denote the plate radius and the gap angle between the cone and plate, respectively. The data (plots) coincide, within experimental uncertainty, with the lines, confirming the uniformity of the LAOS field.

A previous theoretical analysis[13] (based on the Green−Kubo theorem) predicted strong coupling between the LAOS field and the conformational distribution function of PI chains, and this coupling should result in oscillatory decay of the relaxational current $I_{relax}(t)$ under a constant (rectangular) electric field. A summary of the analysis is given in the Supporting Information. Here, we test this prediction for the rheo-dielectric behavior of the linear and star PI solutions (containing no particle) under the *uniform* LAOS field (implicitly assumed in the analysis). The adsorption current (AdC) method[12,20] was utilized to obtain $I_{relax}(t)$ as the relaxational part of the adsorption current under the rectangular

dx.doi.org/10.1021/ma402100t | *Macromolecules* 2014, 47, 246−255

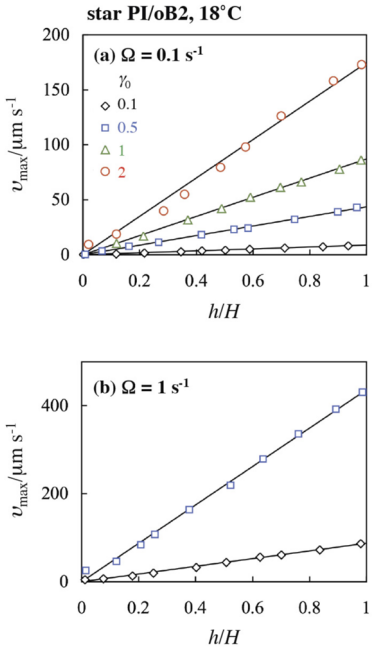

Figure 9. Maximum velocity v_{max} of particles dispersed in the star PI solution. v_{max} is plotted against the particle height h from the fixed plate normalized by the gap H. Solid lines show the maximum velocity realized for uniform oscillatory strain field.

electric field. (Standard measurements utilizing the oscillatory electric field were not attempted for the reason explained later.)

Figures 10 and 11 show the $I_{relax}(t)$ data obtained for the linear and star PI solutions, respectively. For comparison, the

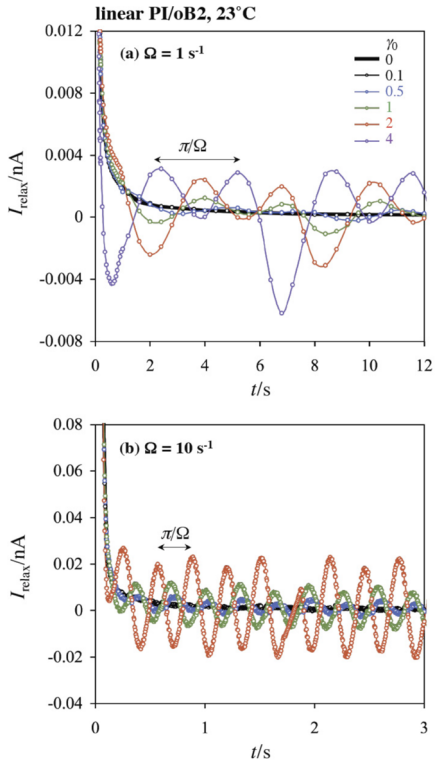

Figure 10. Relaxational current $I_{relax}(t)$ measured for the linear PI solution under the LAOS condition as indicated. Thick solid curve shows the $I_{relax}(t)$ data at equilibrium (without LAOS).

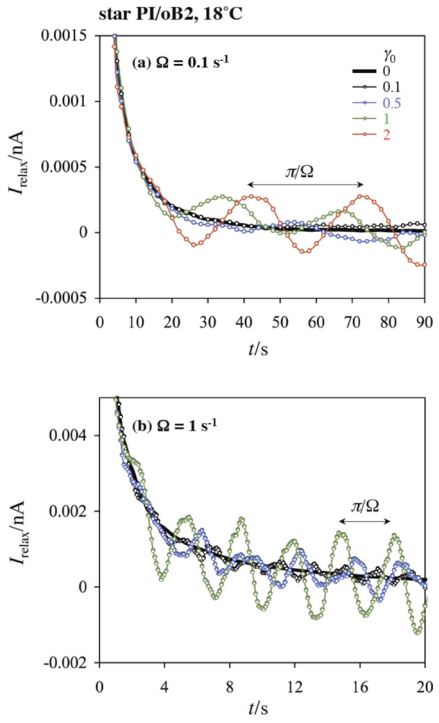

Figure 11. Relaxational current $I_{relax}(t)$ measured for the star PI solution under the LAOS condition as indicated. Thick solid curve shows the $I_{relax}(t)$ data at equilibrium (without LAOS).

$I^{eq}_{relax}(t)$ data at equilibrium (without LAOS) are shown with the thick solid curves. (Those $I^{eq}_{relax}(t)$ data were utilized to evaluate $\Delta\varepsilon'(\omega)$ and $\varepsilon''(\omega)$ shown in Figures 1 and 2.) Clearly, the $I^{eq}_{relax}(t)$ data decays monotonically with time, whereas $I_{relax}(t)$ under LAOS oscillates around $I^{eq}_{relax}(t)$. This oscillation never vanished even at long $t \gg \tau_G(0)$ $(=1/\omega_G(0))$ where $I^{eq}_{relax}(t)$ fully decayed to zero. (No such long time data are shown in Figures 10 and 11 because inclusion of those data compresses the time axis of the plots to disturb visual inspection of the oscillation). $I^{eq}_{relax}(t)$ oscillates with a period of π/Ω in most cases, although the oscillation is not perfectly sinusoidal and thus contributed from harmonics oscillating with different periods (for the higher harmonics of LAOS).

The oscillation of $I_{relax}(t)$ observed under LAOS is intimately related to the oscillation of the conformational distribution function f_{LAOS} coupled with LAOS, as deduced from the previous theoretical analysis.[13] Specifically, the analysis indicates that this oscillation of f_{LAOS} forces $I_{relax}(t)$ to oscillate around a monotonically decaying average, $I^{ave}_{relax}(t) \equiv (\Omega/2\pi) \int_{t-\pi/\Omega}^{t+\pi/\Omega} I_{relax}(t')\, dt'$, as noted in the previous paper[13] and also explained in the Supporting Information of this paper. This oscillatory feature of $I_{relax}(t)$ is consistent with the data in Figures 10 and 11, lending support to the previous analysis. The analysis also suggests that the oscillation includes, in principle, all harmonics of LAOS (having periods $2\pi/p\Omega$ with p = 1, 2, 3, ...) because of the normalization condition for f_{LAOS}, but the oscillation dominantly occurs with the period π/Ω (p = 2) accompanying the squared strain, γ^2 $(=\gamma_0^2 \sin^2\Omega t = \{\gamma_0^2/2\}\{1 - \cos 2\Omega t\})$ if the LASO effect on f_{LAOS} is rather mild; see the Supporting Information. This theoretical argument is also consistent with the experiments, as noted in Figures 12 where the Fourier power spectra $J(\omega)$ of the $\Delta I_{relax}(t) = I_{relax}(t) - I^{eq}_{relax}(t)$ data $(\cong I_{relax}(t) - I^{ave}_{relax}(t)$; oscillatory component of

dx.doi.org/10.1021/ma402100t | Macromolecules 2014, 47, 246−255

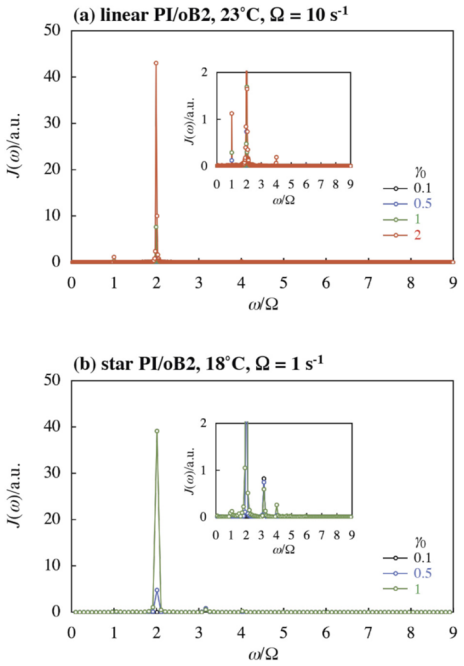

Figure 12. Fourier power spectra $J(\omega)$ calculated from the relaxational current $I_{relax}(t)$ data for the linear and star PI solutions (Figures 10 and 11) at the highest LAOS frequencies Ω examined for respective solutions. $J(\omega)$ is plotted against a normalized angular frequency ω/Ω. The inset magnifies the weak but detectable harmonics.

I_{relax}) are shown for the linear and star PI solutions subjected to fast LAOS (at Ω = 10 and 1 s^{-1}, respectively).

In a very *qualitative* sense, the decay of the average $I^{ave}_{relax}(t)$ becomes faster if the end-to-end fluctuation is accelerated by LAOS, and *vice versa*, as explained in the Supporting Information. The data in Figures 10 and 11 suggest no significant acceleration of the decay of $I^{ave}_{relax}(t)$ under LAOS, which is in harmony with the results obtained under steady shear (Figure 5).

It may look tempting to make detailed analysis of the $I_{relax}(t)$ data under LAOS (and their power spectra) for extracting quantitative molecular information from those data. Such analysis is interesting and important but, unfortunately, highly complicated to be achieved rigorously, because the conformational distribution function f_{LAOS} is coupled with LAOS to oscillate with time. This oscillation leads to oscillatory decay of the I_{relax} data, but the oscillatory parts of f_{LAOS} and I_{relax} are not in proportion to each other and a relationship of these parts depends on the functional form of f_{LAOS}, as explained in Supporting Information on the basis of the previous analysis.[13] In other words, f_{LAOS} cannot be straightforwardly and uniquely determined from the I_{relax} data, unless we make some approximation. For this reason, this study attempts no detailed analysis of the data shown in Figures 10-12. Development of the method of such detailed analysis, based just on the Green−Kubo theorem but with some harmless approximation, is considered to be an interesting and important subject of future study.

3.3.2. Comment for Measurements with Sinusoidal Electric Field. In relation to the above complication in the analysis of the data obtained for the constant (rectangular) electric field, one might consider that the apparent dielectric loss $\varepsilon''(\omega)$ under LAOS is to be measured with the standard method utilizing the sinusoidal electric field. In fact, such $\varepsilon''(\omega)$ data have been reported and discussed in literature.[36,37] However, these $\varepsilon''(\omega)$ data are equivalent to the Fourier transformation of $I_{relax}(t)$ that exhibits the oscillatory decay (cf. Figures 10 and 11) and are affected by the interference between the LAOS and electric fields (no similar interference occurs under steady shear): This interference provides $\varepsilon''(\omega)$ with an *artificial* relaxation process that is in a sense similar to the resonance at $\omega = p\Omega$ with p = 1, 2, ... (see eqs 23 and 24 in ref 13). Furthermore, the dielectric relaxation intensity $\Delta\varepsilon$ evaluated from $\varepsilon''(\omega)$ under LAOS deviates from the real intensity calculated from $\langle R_y^2 \rangle$ averaged during the LAOS period,[13] meaning that the $\varepsilon''(\omega)$ data under LAOS do not include the full/straightforward molecular information on the chain dynamics under LAOS. Analysis of those $\varepsilon''(\omega)$ data is extremely complicated even compared to the analysis of the $I_{relax}(t)$ data under the constant electric field. Specifically, the usual molecular analysis valid for the $\varepsilon''(\omega)$ data at equilibrium[22,23] cannot apply to the $\varepsilon''(\omega)$ data under LAOS.[36,37] This analysis, if made for the data under LAOS, should result in a physically unreasonable molecular picture. For this reason, this study did not attempt to measure/analyze $\varepsilon''(\omega)$ under LAOS.

4. CONCLUDING REMARKS

In this study, we have examined the rheo-dielectric behavior of entangled solutions of linear and star PI chains subjected to steady shear. The particle tracking velocimetry confirmed uniformity of the flow field (lack of shear banding/secondary flow) in the range of Weissenberg number Wi ($=\dot{\gamma}\tau_G(0)$) examined. For linear PI examined at Wi < 7, the dielectric behavior was hardly affected by the steady shear, whereas the viscosity η exhibited considerable thinning. In contrast, for star PI, the dielectric relaxation was moderately accelerated by the steady shear in a similar range of Wi (<8.5), but this acceleration was less significant compared to the thinning of η. These rheo-dielectric features, observed under *uniform* steady shear, suggest an essential difference(s) of the dynamics of the linear and star PI chains under steady fast shear. This difference possibly reflects a difference of the constraint release effect for those chains at equilibrium/under flow and may be also related to anisotropy of the segmental friction that would emerge if the chains are highly oriented. The difference of the rheo-dielectric behavior of the linear and star chains deserves further attention.

The rheo-dielectric behavior of the linear and star PI chains was examined also under LAOS. The uniformity of the LAOS field was confirmed from the particle tracking velocimetry. The relaxational current under a constant (rectangular) electric field exhibited oscillation around the monotonically decaying average current, and the main period of oscillation was close to π/Ω with Ω being the LAOS angular frequency. This behavior lent support to the previous analysis based on the Green−Kubo theorem. The decay of the average current was not significantly affected by LAOS, which was in harmony with the behavior observed under steady shear.

■ ASSOCIATED CONTENT

Supporting Information

Analysis of linear viscoelastic and dielectric behavior of PI/oB2 solutions, example of tube model calculation for rheo-dielectric response under steady shear, and summary of Green−Kubo analysis for rheo-dielectric response under LAOS.This material is available free of charge via the Internet at http://pubs.acs.org.

AUTHOR INFORMATION

Corresponding Author

*E-mail: (H.W.) hiroshi@scl.kyoto-u.ac.jp.

Notes

The authors declare no competing financial interest.

ACKNOWLEDGMENTS

The authors express their sincere thanks and appreciation for Dr. R. Graham at University of Nottingham who kindly allowed us to utilize his GLaMM calculation results in the Supporting Information. This work was partly supported by the Grant-in-Aid for Scientific Research (A) from MEXT, Japan (Grant No. 24245045), Grant-in-Aid for Scientific Research (B) from JSPS, Japan (Grant No. 23350113), Grant-in-Aid for Scientific Research (C) from JSPS, Japan (Grant No. 24550135), and the Research Fellowships of JSPS for Young Scientists.

REFERENCES

(1) Doi, M.; Edwards, S. F. *The Theory of Polymer Dynamics*; Clarendon: Oxford, U.K., 1986.

(2) McLeish, T. C. B. *Adv. Phys.* **2002**, *51*, 1379.

(3) Watanabe, H. *Prog. Polym. Sci.* **1999**, *24*, 1253.

(4) Likhtman, A. E. Viscoelasticity and molecular rheology. In *Polymer Science: A Comprehensive Reference*, 1st ed.; Möeller, M., Matyjaszewski. K., Eds.; Elsevier: Amsterdam, 2012; Vol. *1*: Basic Concepts and Polymer Properties.

(5) Pearson, D. S.; Herbolzheimer, E.; Grizzuti, N.; Marrucci, G. *J. Polym. Sci., Part B: Polym. Phys.* **1991**, *29*, 1589.

(6) Ianniruberto, G.; Marrucci, G. *J. Non-Newtonian Fluid Mech.* **1996**, *65*, 241.

(7) Mead, D. W.; Larson, R. G.; Doi, M. *Macromolecules* **1998**, *31*, 7895.

(8) Milner, S. T.; McLeish, T. C. B.; Likhtman, A. E. *J. Rheol.* **2001**, *45*, 539.

(9) (a) Likhtman, A. E.; Graham, R. S. *J. Non-Newtonian Fluid Mech.* **2003**, *144*, 1. (b) Graham, R. S.; Likhtman, A. E.; McLeish, T. C. B.; Milner, S. T. *J. Rheol.* **2003**, *47*, 1171.

(10) Masubuchi, Y.; Watanabe, H.; Ianniruberto, G.; Greco, F.; Marrucci, G. *Nihon Reoroji Gakkaishi (J. Soc. Rheol. Jpn.)* **2004**, *32*, 197.

(11) Furuichi, K.; Nonomura, C.; Masubuchi, M.; Watanabe, H.; Ianniruberto, G.; Greco, F.; Marrucci, G. *Rheol. Acta* **2008**, *47*, 591.

(12) Watanabe, H.; Ishida, S.; Matsumiya, Y. *Macromolecules* **2002**, *35*, 8802.

(13) Uneyama, T.; Masubuchi, Y.; Horio, K.; Matsumiya, Y.; Watanabe, H.; Pathak, J. A.; Roland, C. M. *J. Polym. Sci., Part B: Polym. Phys.* **2009**, *47*, 1039.

(14) Tapadia, P.; Wang, S. Q. *Phys. Rev. Lett.* **2003**, *91*, 198301.

(15) Tapadia, P.; Ravindranath, S.; Wang, S. Q. *Phys. Rev. Lett.* **2006**, *96*, 196001.

(16) Wang, S. Q.; Ravindranath, S.; Boukany, P. E. *Macromolecules* **2011**, *44*, 183.

(17) (a) Watanabe, H.; Ishida, S.; Matsumiya, Y.; Inoue, T. *Macromolecules* **2004**, *37*, 1937. (b) Watanabe, H.; Ishida, S.; Matsumiya, Y.; Inoue, T. *Macromolecules* **2004**, *37*, 6619.

(18) Sawada, T.; Qiao, X.; Watanabe, H. *Nihon Reoroji Gakkaishi (J. Soc. Rheol. Jpn.)* **2007**, *35*, 11.

(19) Watanabe, H.; Sato, T.; Osaki, K. *Macromolecules* **1996**, *29*, 104.

(20) Watanabe, H.; Matsumiya, Y.; Inoue, T. *Macromolecules* **2002**, *35*, 2339.

(21) Ferry, J. D. *Viscoelastic Properties of Polymers*, 3rd ed.; Wiley: New York, 1980.

(22) Watanabe, H. *Macromol. Rapid Commun.* **2001**, *22*, 127.

(23) Watanabe, H. *Polym. J.* **2009**, *41*, 929.

(24) Cole, R. *J. Chem. Phys.* **1965**, *42*, 637.

(25) Matsumiya, Y. *Nihon Reoroji Gakkaishi (J. Soc. Rheol. Jpn.)* **2011**, *39*, 197.

(26) Watanabe, H. *Nihon Reoroji Gakkaishi (J. Soc. Rheol. Jpn.)* **2012**, *40*, 209.

(27) Matsumiya, Y.; Kumazawa, K.; Nagao, M.; Urakawa, O.; Watanabe, H. *Macromolecules* **2013**, *46*, 6067. See also the Supporting Information of this paper.

(28) Watanabe, H.; Sawada, T.; Matsumiya, Y. *Macromolecules* **2006**, *39*, 2553.

(29) Qiao, X.; Sawada, T.; Matsumiya, Y.; Watanabe, H. *Macromolecules* **2006**, *39*, 7333.

(30) (a) The flow instability due to the edge fracture and/or shear banding could be partly avoided *if* we increase the shear rate gradually (rate-ramping protocol).[30b] However, we did not make such rate-ramping in our rheo-dielectric test, and the edge fracture propagated inward to disturb the test for the linear PI solution at $\dot{\gamma} = 0.6\ s^{-1}$ thereby giving no reliable rheo-dielectric data at this $\dot{\gamma}$, although the solution was not in the highly entangled regime ($M/M_e > 20$) where the shear banding has been claimed[16] and subjected to controversy.[30c] (b) Boukany, P. E.; Wang, S. Q. *Macromolecules* **2010**, *43*, 6950. (c) Li, Y.; Hu, M.; McKenna, G. B.; Dimitriou, C. J.; McKinley, G. H.; Mick, R. M.; Venerus, D. C.; Archer, L. A. *J. Rheol.* **2013**, *57*, 1411.

(31) Ianniruberto, G.; Marrucci, G. *J. Non-Newtonian Fluid Mech.* **2000**, *95*, 363.

(32) Uneyama, T.; Horio, K.; Watanabe, H. *Phys. Rev. E.* **2011**, *83*, 061802.

(33) Ianniruberto, G.; Brasiello, A.; Marrucci, G. *Macromolecules* **2012**, *45*, 8058.

(34) Sugimoto, M.; Suzuki, Y.; Hyun, K.; Ahn, K. H.; Ushioda, T.; Nishioka, A.; Taniguchi, T.; Koyama, K. *Rheol. Acta* **2006**, *46*, 33.

(35) Hyun, K.; Wilhelm, M. *Macromolecules* **2009**, *42*, 411.

(36) Höfl, S.; Kremer, F.; Spiess, H. W.; Wilhelm, M.; Kahle, S. *Polymer* **2006**, *47*, 7282.

(37) Capaccioli, S.; Prevosto, D.; Best, A.; Hanewald, A.; Pakula, T. *J. Non-Cryst. Solids* **2007**, *353*, 4267.